Long-Term Behavior of Cloud Systems in TOGA COARE and Their Interactions with Radiative and Surface Processes. Part II: Effects of Ice Microphysics on Cloud–Radiation Interaction

XIAOQING WU, WILLIAM D. HALL, WOJCIECH W. GRABOWSKI, MITCHELL W. MONCRIEFF, WILLIAM D. COLLINS, AND JEFFREY T. KIEHL

National Center for Atmospheric Research, Boulder, Colorado*

(Manuscript received 9 March 1998, in final form 4 December 1998)

ABSTRACT

A two-dimensional cloud-resolving model with a large domain is integrated for 39 days during the Tropical Ocean Global Atmosphere Coupled Ocean–Atmosphere Response Experiment (TOGA COARE) to study the effects of ice phase processes on cloud properties and cloud radiative properties. The ice microphysical parameterization scheme is modified based on microphysical measurements from the Central Equatorial Pacific Experiment. A nonlocal boundary layer diffusion scheme is included to improve the simulation of the surface heat fluxes. The modified ice scheme produces fewer ice clouds during the 39-day simulation. The cloud radiative properties show significant improvement and compare well with various observations. Both the 39-day mean value (202 W m^{-2}) and month-long evolution of outgoing longwave radiative flux from the model are comparable with satellite observations. The 39-day mean surface shortwave cloud forcing is -110 W m^{-2}, consistent with other estimates obtained for TOGA COARE. The 39-day mean values of surface net longwave, shortwave, latent, and sensible fluxes are -46.2, 182.9, -109.9, and -7.8 W m^{-2}, respectively, in line with the IMET buoy data (-54.6, 178.2, -102.7, and -10.6 W m^{-2}).

The offline radiation calculations as well as the cloud-interactive radiation simulations demonstrate that a doubled effective radius of ice particles and enhanced shortwave cloud absorption strongly affect the radiative flux and cloud radiative forcing but have little impact on the cloud properties. The modeled albedo is sensitive to the effective radius of ice particles and/or the shortwave cloud absorption in the radiation scheme. More complete satellite observations and theoretical studies are required to fully understand the physical processes involved.

The results suggest that the ice microphysical parameterization plays an important role in the long-term simulation of cloud properties and cloud radiative properties. Future field observations should put more weight on the microphysical properties, cloud properties, and high-quality radiative properties in order to further improve the cloud-resolving modeling of cloud systems and the understanding of cloud–radiation interaction.

1. Introduction

In Part I of this paper (Wu et al. 1998, hereafter WGM), a two-dimensional finescale simulation was performed for 39 days during the Tropical Ocean Global Atmosphere Coupled Ocean–Atmosphere Response Experiment (TOGA COARE). Its goal was to produce cloud-scale properties that cannot be accurately measured on large spatial and temporal scales. It is demonstrated that the use of observed evolving large-scale forcing in a cloud-resolving model (CRM) can simulate the evolution of ensemble mean of cloud properties, cloud radiative forcing, and surface fluxes over a large domain for a long time period. The key is that the interaction among microphysics, radiation, surface flux, and turbulence is explicitly treated by the resolved cloud-scale dynamics in the CRM.

It is important to note that the CRM approach is semidiagnostic in the sense that the domain-averaged temperature and moisture fields are affected by the large-scale forcing, but cloud properties (e.g., ice water content and liquid water content) are simulated without the influence of large-scale condensate forcing. The microphysical parameterization and lateral boundary conditions used in the CRMs will certainly affect the simulation of these fields. Since the long-term cloud condensate data is not available from observations, the direct comparison between models and observations is impossible at present. However, the comparison of outgoing longwave radiative flux (OLR) between the 39-

* The National Center for Atmospheric Research is sponsored by the National Science Foundation.

Corresponding author address: Dr. Xiaoqing Wu, NCAR, P.O. Box 3000, Boulder, CO 80307.
E-mail: xiaoqing@ncar.ucar.edu

day simulation and satellite observations in WGM suggests that the amount of model-produced cloud condensate may be too large or the vertical distribution of cloud condensate is not accurate, which in turn is directly linked to the microphysical parameterizations.

Many previous studies have been conducted on the effects of microphysics on the simulation of tropical and midlatitude cloud systems such as squall lines using the cloud-resolving models (e.g., Yoshizaki 1986; Nicholls 1987; Fovell and Ogura 1988; Tao and Simpson 1989; Dudhia 1989; McCumber et al. 1991; Chin 1994; Ferrier et al. 1995; Tao et al. 1995; Krueger et al. 1995; Fu et al. 1995; Wu and Moncrieff 1996; Liu et al. 1997). The focus in these studies is the effects of ice phase processes on the organization and structure of cloud systems. Although the structure of squall line is basically controlled by the dynamics, ice microphysics plays an important role for a realistic simulation of stratiform and precipitation parts of squall lines in CRMs. McCumber et al. (1991) and Ferrier et al. (1995) compared the performance of several ice parameterizations ranging from two-class ice (Cotton et al. 1982), to three-class ice (Lin et al. 1983; Rutledge and Hobbs 1983), to four-class ice (Ferrier 1994) in the simulations of tropical squall line and nonsquall cloud clusters. These two papers showed that very different ensemble mean vertical hydrometeor profiles were produced by different ice schemes. They went on to point out that the use of bulk ice parameterizations in cloud models might be case dependent. Note that all of these cloud-resolving modeling studies were short-term (several hours) case studies.

Work has also been conducted to study the effects of cloud microphysics on large-scale circulation and climate using the general circulation models (GCMs). Ramanathan et al. (1983) found that upper-tropospheric temperature and wind fields were more realistically simulated with the inclusion of variable cirrus cloud emissivity. Slingo (1987) included a fractional cloud cover scheme in the European Centre for Medium-Range Weather Forecasts medium-range forecast model and demonstrated that tropical and extratropical cloudiness can be fairly well predicted. Heymsfield and Donner (1990) developed a parameterization scheme that represents ice water content using the vertical velocity and temperature at grid points in a GCM. The comparison between parameterized and aircraft-observed ice water contents showed reasonable agreement in the Tropics and midlatitude. Recently, Fowler et al. (1996) incoporated a more complicated bulk cloud microphysics scheme [based on Lin et al. (1983) and Rutledge and Hobbs (1983)], which was used in cloud-resolving models, into a GCM. They showed that the GCM with the direct implementation of microphysical processes produced a more realistic hydrologic cycle and radiation budgets. Note that, besides the cloud microphysical parameterization, cloud-scale processes have to be represented by the resolved variables in these GCMs.

The objective of this paper is to improve the simulation of cloud fields and demonstrate the effects of ice phase processes on cloud–radiation interaction. A unique feature is that the cloud-resolving model resolves cloud dynamics, has a large domain, and was run for a month-long period. The strategy is to perform sensitivity tests based on microphysical measurements from the Central Equatorial Pacific Experiment (CEPEX), which was conducted just after TOGA COARE during March and April 1993 (Williams 1993). The model-produced cloud radiative properties can be quantitatively compared with satellite observations such as OLR and albedo.

The paper is organized as follows. In the next section, the experimental design and modification of parameters in the ice parameterization scheme will be described. Section 3 examines the effects of the modified ice parameterization scheme on thermodynamical fields. The effects of modified ice scheme on cloud properties and cloud radiative properties are presented in section 4. Offline sensitivity calculations using the radiative transfer model and the model-produced cloud-scale fields are discussed in section 5. The results are summarized in section 6.

2. Experimental design and modification of model physics

a. Experimental design and observed large-scale forcing

The numerical model and the design of the numerical experiments are the same as in WGM. The National Center for Atmospheric Research Community Climate Model 2 radiation model (Kiehl et al. 1994) was incorporated in a two-dimensional version of the Clark–Hall cloud model (Clark et al. 1996). A Kessler (1969) bulk warm rain parameterization and a Koenig and Murray (1976) bulk ice parameterization are used. The surface fluxes of sensible and latent heat are calculated using the evolving sea surface temperature and a simplified version of the TOGA COARE surface flux algorithm (Fairall et al. 1996). The subgrid-scale mixing is parameterized using the first-order eddy diffusion method of Smagorinsky (1963). To improve the simulation of the boundary layer structure, a nonlocal boundary layer diffusion scheme (Troen and Mahrt 1986; Holtslag and Moeng 1991; Hong and Pan 1996) is included assuming a constant boundary layer height of 600 m.

The x axis of the model is aligned east–west in the two-dimensional x–z domain, which is 900 km long by 40 km deep. The horizontal grid length is 3 km. A stretched grid in the vertical with 52 levels (100 m at the surface, 550–850 m between 5 and 12 km, and 1500 m at the model top) is used, requiring a time step of 15 s. Free-slip, rigid bottom and top boundary conditions are applied together with a gravity wave absorber in the

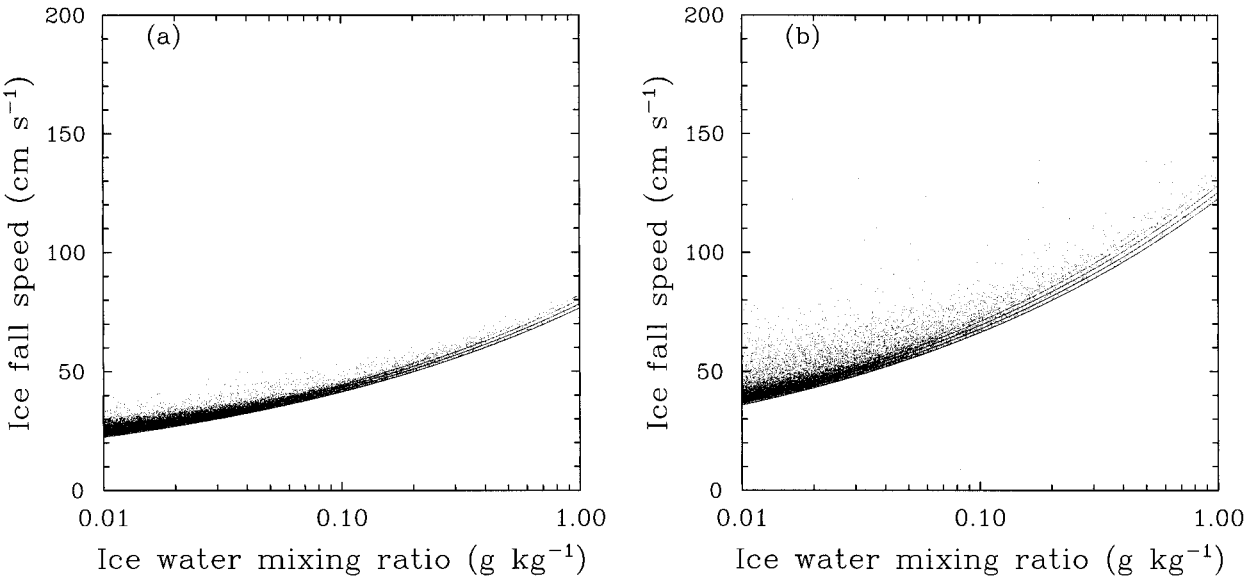

FIG. 1. Ice fall speed (cm s^{-1}) vs ice water mixing ratio (g kg^{-1}) from models (a) E0 and (b) M0 during 10–13 Dec 1992.

uppermost 14 km of the domain. There is no parameterized surface momentum flux.

Because of approximations applied in the radiation transfer model, only mixing ratios for cloud water and type-A ice (see next section for the definition) are used in the radiation model when the interactive radiation scheme is applied. Effective radii of water droplet and ice crystals (required by the radiation scheme) are assumed to be 10 and 30 μm, respectively. Radiation calculations are performed every 150 s, with the most recent tendencies applied between consecutive calculations. A detailed description for the parameterization of cloud optical properties in the radiation model can be found in Kiehl et al. (1998).

A new 39-day (5 December 1992–12 January 1993) simulation with modified physics will be referred as M0 in the following sections. The 39-day simulation presented in Part I of this paper was labeled E0. The large-scale forcing and horizontal wind profiles for M0 are the same as E0, which is obtained from the objectively analyzed TOGA COARE sounding data (Lin and Johnson 1996). The use of a nonlocal boundary layer diffusion scheme and the modification of ice fall speed are the only two changes in M0. The simulation with only boundary layer modification (not presented in this paper) showed the improvement of the surface fluxes and the slight increase of the ice water content because of the increase of surface fluxes.

b. Modification of ice microphysics

The basic assumption within the ice microphysical scheme of Koenig and Murray (1976) is that the cloud microphysical characteristics can be represented in bulk form by a minimum number of variables. The parameterization scheme combines known details of single hydrometeor growth and terminal fall speed information with known observational ice particle shapes and spectral characteristics to yield a predictive system for the development of precipitation within the cloud model. Two types of particles, type-A ice and type-B ice, are considered in this scheme. Unlike other two-class ice schemes, both the mixing ratio and the number concentration are predicted for type-A and type-B ice particles. The physical equations used by each class are the same except for the initial particle size and the sources. Type-A ice particles represent particles that are initially small and are created by either heterogeneous sorption nucleation of ice crystals above -40°C or homogeneous freezing of cloud droplets at temperature below -40°C. Type-B ice particles represent particles that are initially larger and form when a raindrop freezes after collision with a type-A ice particle.

It is assumed that a given ice category falls with the velocity defined as a terminal velocity of an ice particle of the averaged mass. The averaged mass is defined as the ratio between the ice mixing ratio and ice number concentration. The particle size–velocity relationship is based upon water droplet formulas with ice particle correction factors ranging from 0.2 to 0.8 depending on ambient temperature and mean mass. The result from the original scheme showed a systematic bias that underestimated the sedimentation flux of ice particles based on CEPEX size spectra measurements (McFarquhar and Heymsfield 1996). Figure 1a shows a scatter diagram of the type-A ice fall speed against the ice water mixing ratio using the original ice scheme from E0. Note that the CEPEX measurements were taken within the ambient temperatures ranged between -70° and -20°C. There is no measurement in strong updraft

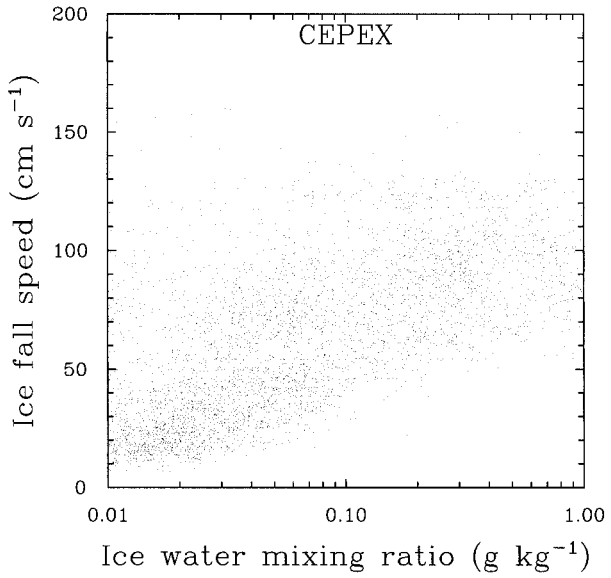

FIG. 2. Ice fall speed (cm s^{-1}) vs ice water mixing ratio (g kg^{-1}) from CEPEX.

cores. The type-B ice (graupel) mainly appears in the vicinity of convective updrafts. The ice fall speed is clearly too small when compared with the ice fall speed from the CEPEX observations (Fig. 2).[1]

Because the total mass of water substance is conserved, the lower sedimentation flux of ice particles results in a longer ice residence time and higher ice water content. In the modified scheme, a constant correction factor for all ice particle size of 0.8 is used for the fall speeds, which would provide an upper limit of what one could normally use. The modified fall speed is more representative of ice pellets and frozen droplets instead of dendritic or columnar ice crystals. The modified scheme results in a more reasonable relationship between the ice fall speed and the ice water mixing ratio as shown in Fig. 1b. The cloud radiative properties from the new 39-day simulation (M0) with the modified ice parameterization scheme is in better agreement with the satellite observations as shown in section 4.

The CEPEX measurements show much more scatter than either the M0 or the E0. It should be mentioned that some bulk ice schemes result in no scatter at all (e.g., Lin et al. 1983, Fig. 2 therein). This points to the general problem of the representation of the ice particle shape and size distribution assumed by any ice parameterization scheme, since ice particles are extremly complex in nature and cannot be completely described by simple functions that parameterizations are built upon. Current parameterization only uses one predominant characteristic based upon the ratio of mixing ratio and number concentration.

[1] The ice fall speed (v_i) is derived from the size spectra as measured by the Particle Measuring Systems' two-dimensional cloud probe. In the v_t calculations, assumptions are made about ice particle mass based on the ice particle size spectra. The v_t in Fig. 2 represents the mass-weighted mean of the size distributions.

3. Thermodynamical fields

a. Temperature and moisture fields

As a first test of the model performance, Fig. 3 presents the 39-day mean profiles of the differences between model-produced and observed temperature, water vapor mixing ratio, and relative humidity. For all three variables M0 is a considerable improvement over E0. The temperature, water vapor mixing ratio, and relative humidity biases for M0 are less than 0.5°C (Fig. 3a), 1.5 g kg^{-1} (Fig. 3b), and 15% (Fig. 3c), respectively. The large temperature difference remaining above 14 km is largely due to the incomplete physics and model resolution for the accurate simulation of height of the tropopause (Grabowski et al. 1996; Wu et al. 1998). These results suggest that the ice phase processes do affect the simulation of thermodynamical fields. Less ice water generated in the domain played a similar role as the large-scale condensate forcing that removed the condensate from the domain during the undisturbed periods. Examination of the 39-day evolution of difference profiles indicates that the bias pattern for M0 remains the same as E0. The biases mainly appear during the undisturbed periods (6–12 January) although their magnitudes are reduced. This leaves the accuracy and availability of large-scale forcing as a major factor responsible for the temperature and moisture biases, an issue that requires further analyses.

b. Surface heat fluxes and precipitation

The model-produced temperature and moisture fields certainly affect the simulation of surface heat fluxes. For the TOGA COARE surface flux algorithm used in the CRM, the sensible and latent heat fluxes are proportional to the potential temperature difference and water vapor difference between the first level (50 m) of the model and the surface, respectively. Figure 4 shows the 39-day evolution of potential temperature and water vapor gradients between the first level of the model and the surface, and the wind speed at the first level of the model from observations, M0 and E0, respectively. The potential temperature gradient from E0 is clearly much larger than the observed value (Fig. 4a) and is responsible for the larger sensible heat flux. The water vapor gradient from E0 generally agrees with observations except toward the end of the simulation when the water vapor gradient is smaller than the observation (Fig. 4b). This contributes to the smaller 39-day mean latent heat flux. The 39-day evolution of wind speed from M0 and E0 generally follows observations (Fig. 4c) as expected with the wind relaxation technique employed.

The addition of vertical mixing by a nonlocal bound-

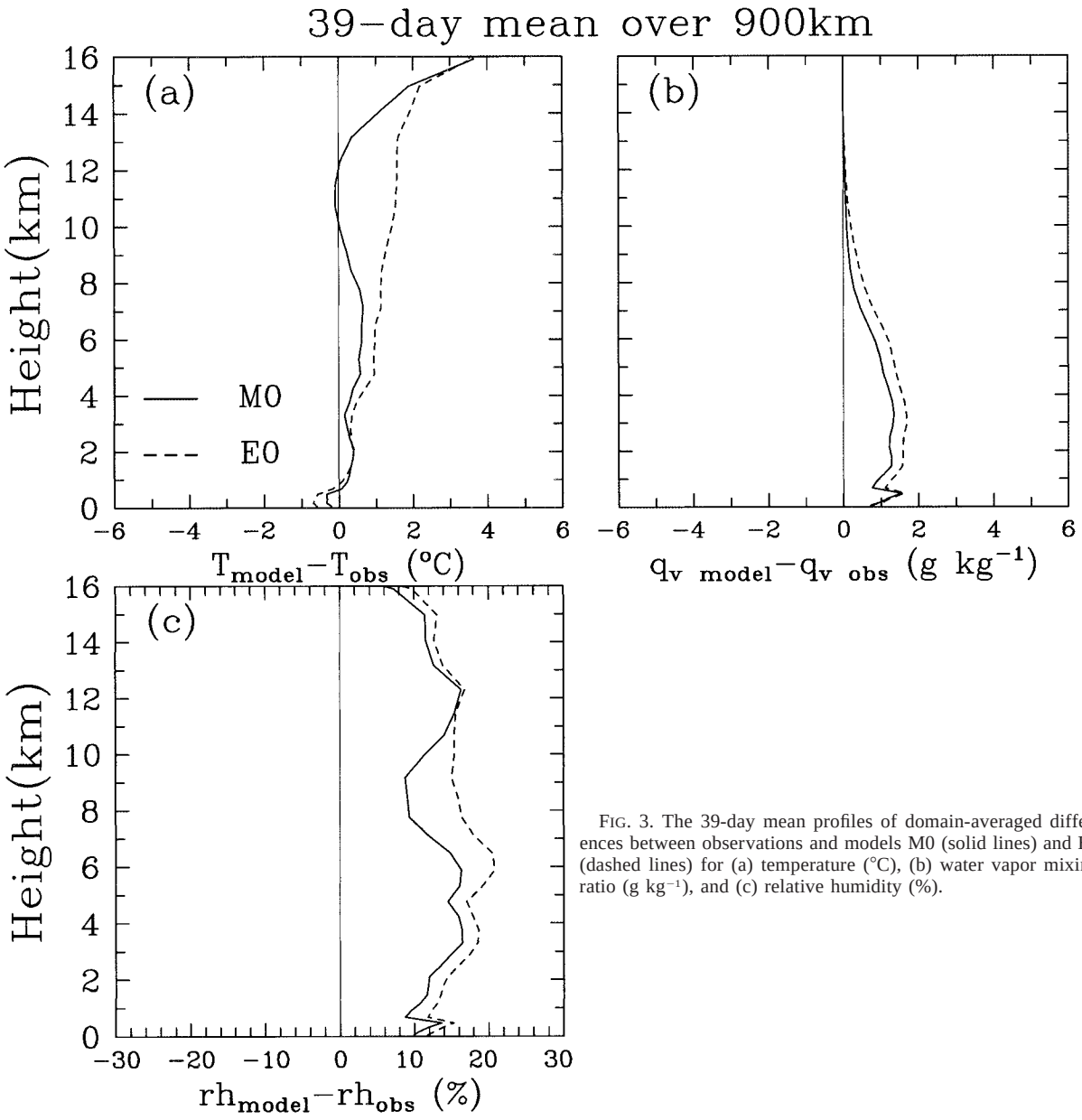

FIG. 3. The 39-day mean profiles of domain-averaged differences between observations and models M0 (solid lines) and E0 (dashed lines) for (a) temperature (°C), (b) water vapor mixing ratio (g kg^{-1}), and (c) relative humidity (%).

ary layer diffusion scheme in the CRM clearly improves the potential temperature gradient in M0, which is generally consistent with observations (Fig. 4a). The sensible heat flux from M0 (Fig. 5a) is closer to the observation than from E0 (Fig. 10 in WGM). The 39-day mean of sensible heat flux from M0 is 7.8 W m^{-2} compared to 13.3 W m^{-2} from E0 and the observed value of 9.2 W m^{-2}. The water vapor gradient from M0 is generally larger than that from E0 with the large increase toward the end of the simulation. This suggests that the addition of the vertical mixing has a small effect on the water vapor field. The increase of water vapor gradient is largely related to the smaller water vapor mixing ratio in M0 compared to E0. The latent heat flux from M0 (Fig. 5b) is closer to observations than that from E0 (Fig. 11 in WGM). The 39-day mean of latent heat flux from M0 is 109.8 W m^{-2} compared to 102.4 W m^{-2} from E0 and 109.8 W m^{-2} from observations. Note that the observed surface heat fluxes are calculated from four buoy datasets, namely the Improved Meteorological surface mooring (IMET) and three TOGA Tropical Atmosphere Ocean Automated Temperature Line Acquisition System moorings.

The impact of the modified ice scheme on the surface precipitation is small, as also demonstrated by previous case studies (e.g., McCumber et al. 1991). Figure 5c shows the 39-day evolution of 6-hourly rainfall rate from M0, which is similar to that from E0 (Fig. 6a in

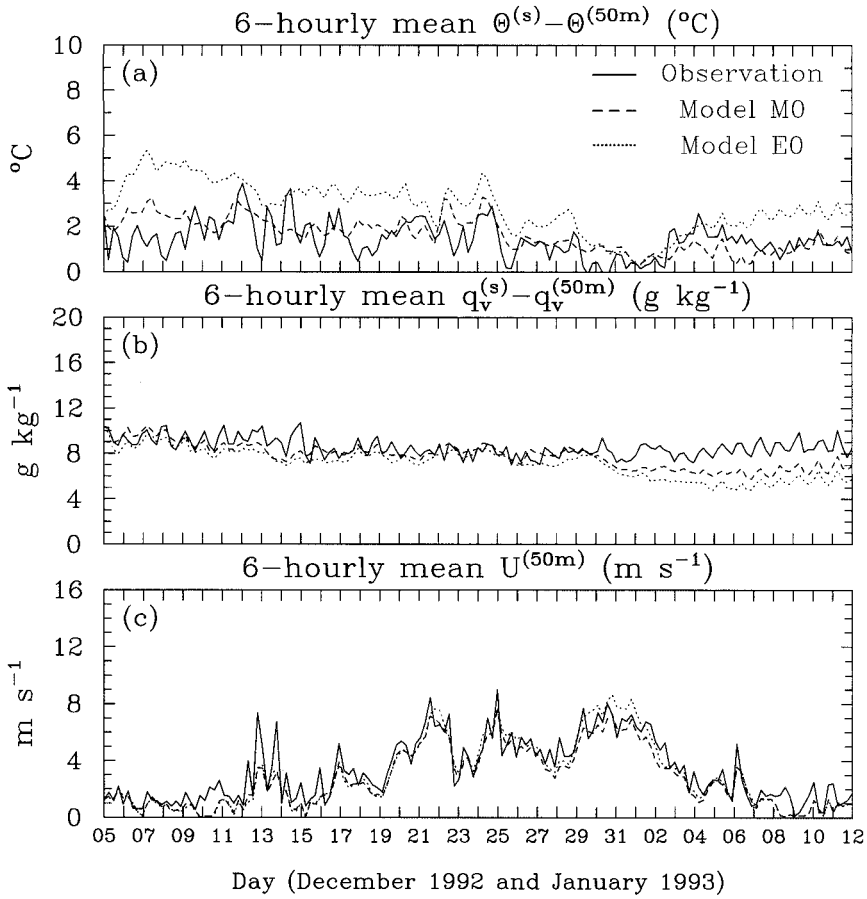

FIG. 4. Evolution of 6-hourly domain-averaged (a) potential temperature (°C) and (b) water vapor mixing ratio (g kg^{-1}) differences between the surface and 50 m, and (c) wind speed (m s^{-1}) at 50 m for observation (solid), model M0 (dashed), and model E0 (dotted).

WGM). The 39-day mean of precipitation is 0.33 mm h^{-1} (equivalent to 229 W m^{-2}) for M0, which is slightly larger than the mean (0.32 mm h^{-1} or 222 W m^{-2}) from E0. The small increase of precipitation is consistent with the small increase of surface latent heat flux.

4. Cloud properties and their influence on radiative fluxes

In this section, cloud properties generated from M0 and E0 are compared in order to demonstrate the effects of ice phase processes on the long-term simulation. Since no measurements of condensate mass were made, the quality of model-generated condensate is evaluated indirectly by comparing the ensemble mean of cloud radiative properties with observations.

a. Cloud mass flux

As in WGM, the total cloud mass flux is calculated over regions where the total condensate (the sum of liquid water, ice water, and rainwater) mixing ratio is equal to, or larger than, 0.1 g kg^{-1}. The positive values define the updraft mass flux, while the negative values represent the downdraft mass flux. Figure 6 presents the 39-day evolution of the mass fluxes from M0. The mass fluxes in M0 are generally similar to those in E0 (Fig. 5 in WGM). The most noticeable difference is the reduction of the upper-tropospheric net cloud mass flux (e.g., around 12 km), which is likely a result of reduced upper-tropospheric ice cloud amount and thus weaker detabilization of anvil clouds by radiative processes. In general, the convective intensity is not significantly affected by the modification in the ice phase representation since the convective intensity mainly responds to the large-scale forcing (e.g., upper-level cooling and low-level moistening).

b. Cloud condensate

Figure 7 shows the 39-day evolution of liquid water path and type-A ice water path from M0 and E0, respectively. The notable difference between two simulations is that the ice water path from M0 is much smaller than the ice water path from E0 during strong convection, and decreases more rapidly from its maxima

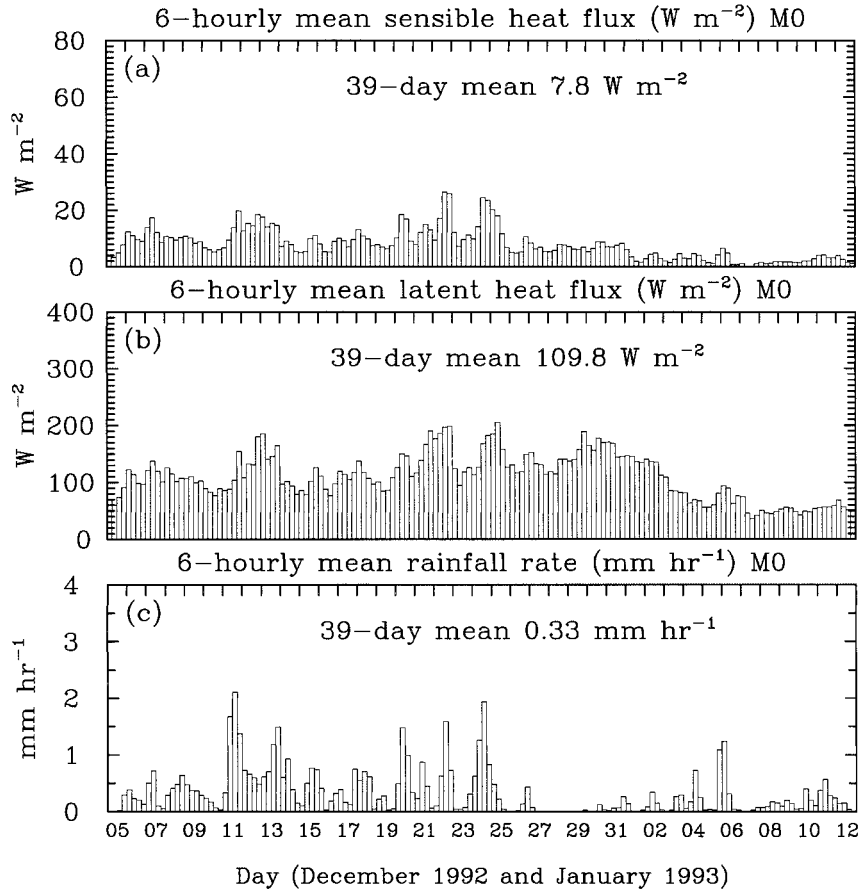

FIG. 5. Evolution of 6-hourly domain-averaged surface (a) sensible heat flux (W m^{-2}), (b) latent heat flux (W m^{-2}), and (c) rainfall rate (mm h^{-1}) from model M0.

(Fig. 7b). The increase of type-A ice fall speed in M0 significantly reduced the type-A ice water path. However, the liquid water path from M0 only slightly differed from E0 because the fall speed of droplets is not changed (Fig. 7a). The difference of cloud properties between M0 and E0 is further examined from the 39-day mean vertical profiles of hydrometeors in Figs. 8a and 8b. A dramatic difference is in the profiles of type-A ice mixing ratio. The peak of type-A ice mixing ratio near 6 km in E0 is greatly reduced. The type-B ice profile is also modified, with a sole peak at the melting level (5 km) in M0. The type-B ice mixing ratio is much smaller than type A. The liquid water mixing ratio is slightly reduced by the modified ice scheme. The rainwater mixing ratio in M0 is little affected.

In the Koenig and Murray scheme, whenever ice particles fall to a region where temperature is larger than 273.15 K, they melt. If the mass of the average particle is less than 10^{-11} kg, there is instantaneous total melting. Otherwise, the rate of change of mass of the average particle is taken to be related to radius and terminal velocity. The major change in the profiles of ice mixing ratio is around 6 km, which is above the melting level. So the profile of rainwater did not change much in M0.

The modified ice parameterization also strongly affects the cloud fraction. Figure 9 shows the 39-day mean vertical profiles of cloud fraction for M0 and E0. At each level, a grid box is defined to be cloudy if the sum of liquid and type-A ice water path exceeds 0.02 kg m^{-2}. The cloud amount is significantly reduced above 4 km in M0 compared to E0 and fewer high clouds are produced in M0.

The 39-day evolution of the vertical profiles of hydrometeors is presented in Fig. 10. The hydrometeor profiles show several distinct episodes of strong convective activity. The melting level is readily identified near 5 km. The peak in total condensate mixing ratio is consistent with the bright band observed at the melting level by the 915-MHz profiler (Gage et al. 1994) and scanning Doppler radars. Gage et al. showed a 3-day (20–22 December 1992) evolution of equivalent reflectivity from the 915-MHz profiler inside the intensive flux array (IFA) of TOGA COARE. Three cloud systems are clearly illustrated during the 3-day period in both the profiler data (Fig. 2 in Gage et al.) and in the model (Fig. 10d). In each cloud system a bright band of high reflectivity clearly exists at the melting level near 5 km. The hydrometeor data retrieved from the

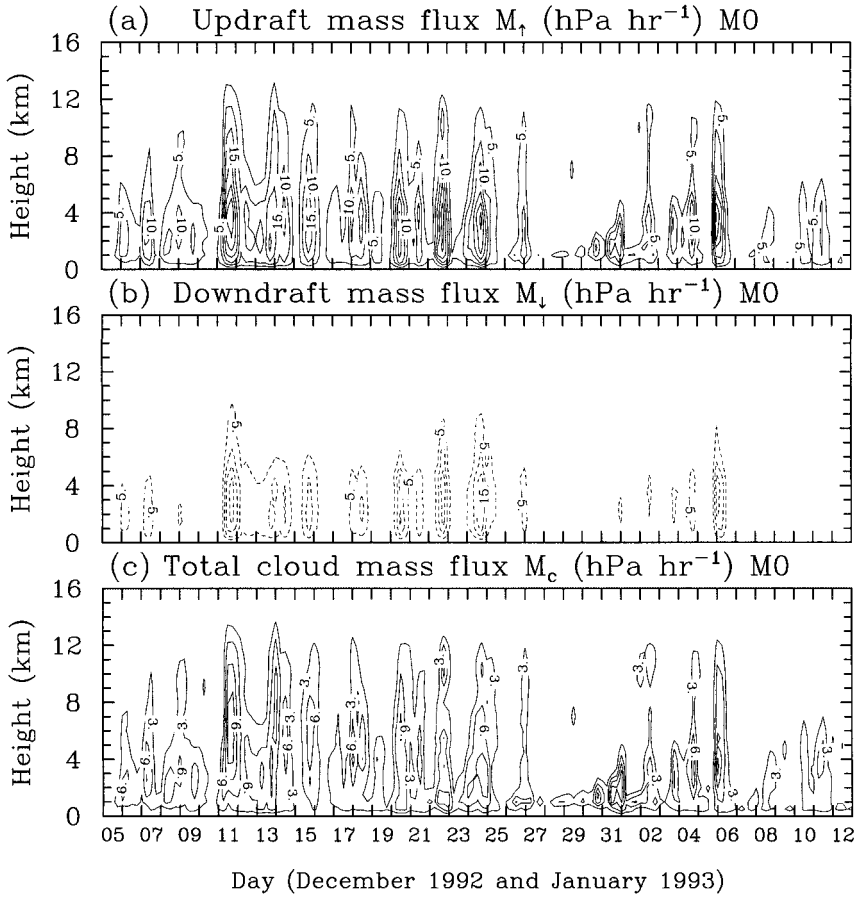

FIG. 6. Evolution of 6-hourly domain-averaged (a) updraft, (b) downdraft, and (c) total cloud mass fluxes calculated as explained in text. Contour interval is (a), (b) 5 hPa h^{-1}, and (c) 3 hPa h^{-1}.

915-MHz profiler will be an excellent condensate dataset for evaluating the model-produced hydrometeors.

The sensitivity of cloud condensate fields to the ice phase processes suggests that more microphysical measurements and theoretical studies are needed to understand physical processes involved in different cloud systems and to properly represent the microphysics in the CRMs. The need for high-quality microphysical data in the development of parameterization has been identified by the Global Energy and Water Cycle Experiment Cloud System Study (GCSS) (GCSS Science Team 1993), but the problem remains.

c. Radiative flux

In this section, the effects of the modified ice scheme on the radiative fluxes are examined and compared to observations. The improvement of the model-produced radiative fluxes is significant. Figure 11 compares the 39-day evolution of OLR and albedo in M0 and E0. The reduction of ice hydrometeor content in M0 compared to E0 results in the decrease of ice water path and infrared absorption and the increase of the OLR during the 39-day period (Fig. 11a). The maximum enhancement of OLR exceeds 40 W m^{-2}. The amplitude of OLR from M0 is closer to observations, as shown in Fig. 12. During the 39-day period, there are several episodes when the values of OLR exceed 200 W m^{-2} in both M0 and the observations. The model-produced OLR shows larger temporal variability than the observations. The 39-day mean of OLR is 202 W m^{-2} from M0, which is 22 W m^{-2} larger than the mean from E0. The 39-day mean of OLR from three observational datasets is 215 W m^{-2} for the flux and cloud data (FC) (e.g., Zhang et al. 1995), 213 W m^{-2} for the *GMS-1* (*Geostationary Meteorological Satellite*) data (Collins et al. 1997), and 215 W m^{-2} for the *GMS-2* data.

The smaller ice water path in M0 than in E0 also reduces the albedo (Fig. 11b). A smaller albedo means less upwelling shortwave flux at the top of the atmosphere. The 39-day mean of albedo is 0.35 from M0 compared to 0.42 from E0. The maximum decrease during the 39-day period is as large as 0.2. The model-produced albedo from M0 is smaller than 0.37 from the FC data, larger than 0.24 from the *GMS-1* data, and larger than 0.31 from the *GMS-2* data (Fig. 13). The

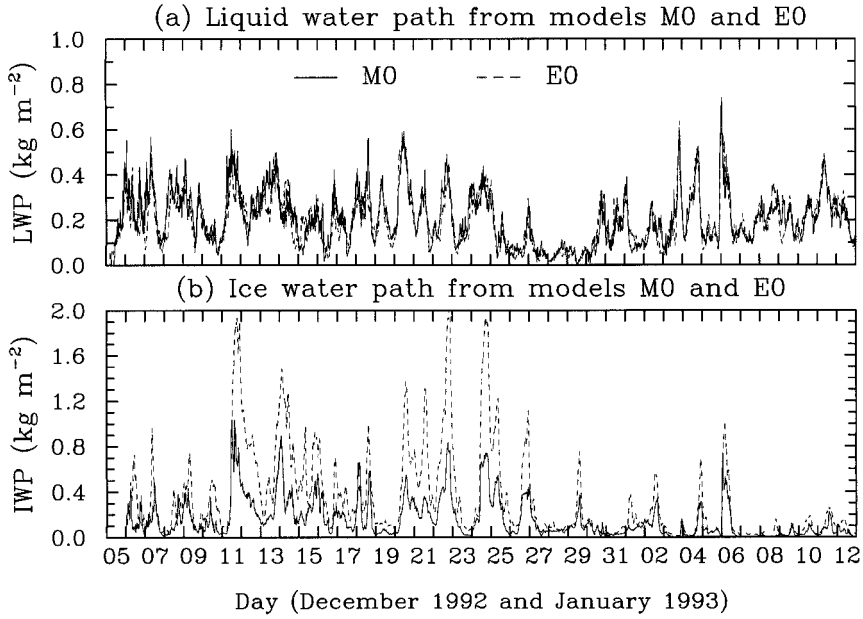

FIG. 7. Evolution of (a) liquid water path and (b) ice water path from models M0 (solid) and E0 (dashed). Units are kg m^{-2}.

offline calculations presented in section 5 will show that the modification of parameters in the radiative transfer model can influence the simulated albedo. The differences among three observational datasets stem from differences in the schemes used for the estimation of broadband fluxes from satellite-measured narrowband radiances. Figure 14 is a scatter diagram of the OLR against the albedo for M0 and observational datasets. Note that the OLR from three datasets is about the same, but the albedo is very different. The slopes of the least squares regression fits of daily mean OLR and albedo are -2.3×10^{-3}, -3.6×10^{-3}, -2.6×10^{-3}, and -3.1×10^{-3} for M0, FC, *GMS-1,* and *GMS-2,* respectively. The slope for E0 is -2.1×10^{-3} (not shown in Fig. 14).

A careful investigation is required to explain why the three methods differ, which is beyond the scope of this paper. Nevertheless, a brief description of these three methods is illuminating. The FC OLR and albedo data are derived from a radiative transfer model using the satellite-measured radiances and the cloud properties obtained from the International Satellite Cloud Climatology Project (e.g., Zhang et al. 1995). The *GMS-1* OLR and albedo data are produced by the calibration of satellite instruments against collocated observations from the National Aeronautics and Space Administration *ER-2* aircraft (Collins et al. 1997). The *GMS-2* OLR and albedo data are estimated by using the empirical narrowband–broadband relationship from simultaneous satellite measurements (e.g., Minnis and Harrison 1984).

d. Radiative heating rate

Figure 15 presents the 39-day mean profiles of shortwave, longwave, and total radiative heating rates averaged over the 900-km domain for M0 and E0. The radiative heating rate is calculated by vertical divergence of radiative fluxes, which is an important quantity in climate modeling. The shortwave heating rate in the upper troposphere is smaller for M0 than for E0 because smaller ice water content is produced in M0, while the heating rate in the lower troposphere is slightly larger for M0 than for E0 (Fig. 15a). The longwave heating profiles show the larger (smaller) cooling for M0 than E0 below (above) 12 km (Fig. 15b). A notable feature in the total radiative heating profiles (Fig. 15c) is the decreased upper-tropospheric radiative instability in M0 compared to E0. The net shortwave and longwave radiative tendency shows the cooling effect throughout the troposphere for M0 with magnitude smaller than 1 K day^{-1}. The cooling effect above 10 km is mainly due to the presence of high ice concentrations during disturbed periods (the magnitude of the net radiative cooling rate reaches 2.5 K day^{-1} at 12 km).

e. Cloud radiative forcing

To examine the large-scale effects of clouds on radiative fluxes, Table 1 lists the 39-day mean shortwave (SWCF) and longwave (LWCF) cloud radiative forcing at the top of the atmosphere (TOA), throughout the atmosphere (ATM) and at the surface (SRF), respectively. The TOA is defined at the top of the model (i.e., 40 km). The cloud radiative forcing is defined as the difference between the total radiative forcing and the radiative forcing corresponding to the clear-sky conditions. Following the method used in Part I, a subset of 10 columns with the maximum values of the OLR was

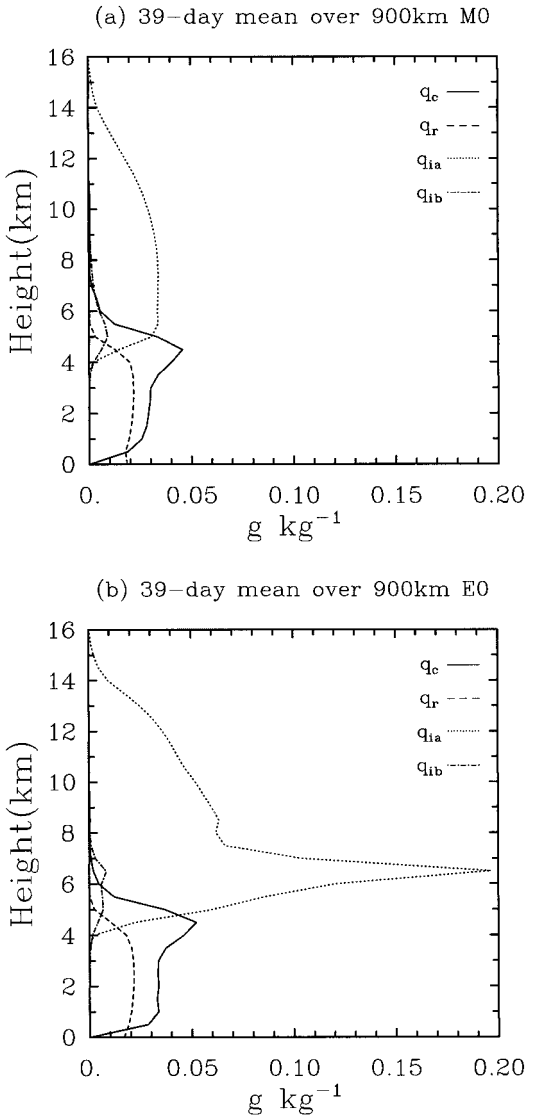

FIG. 8. The 39-day mean profiles of domain-averaged liquid water (solid), rainwater (dashed), type-A ice water (dotted), and type-B ice water (dot–dashed) mixing ratio (g kg^{-1}) from models (a) M0 and (b) E0.

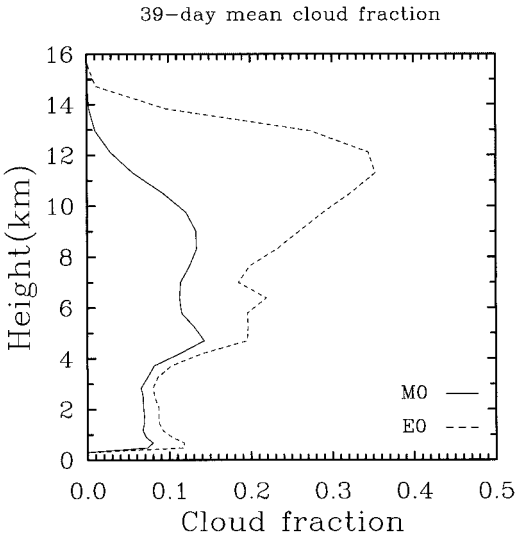

FIG. 9. The 39-day mean vertical profiles of cloud fraction from models M0 (solid) and E0 (dashed).

TABLE 1. Cloud radiative forcing (W m^{-2}) from M0, E0, and FC.

Cloud radiative forcing	M0	E0	FC
$SWCF_{TOA}$	−105	−115	−106
$LWCF_{TOA}$	66	77	60
$SWCF_{ATM}$	5	6	18
$LWCF_{ATM}$	48	62	49
$SWCF_{SRF}$	−110	−121	−98
$LWCF_{SRF}$	18	15	11

selected for every time level. Forcing averaged over these columns was assumed to be representative of the clear-sky conditions (Wu et al. 1998). There is a limitation in this method, particularly during the strongly forced period when clouds cover most of the domain. An offline calculation of radiative fluxes for the clear-sky conditions is performed for the comparison. The cloud radiative forcing obtained from these two methods differs by less than 10 W m^{-2}.

While smaller ice water path produced in M0 results in smaller magnitudes of the SWCF and LWCF at the TOA compared to E0, the sum of SWCF and LWCF is almost the same for M0 (−39 W m^{-2}) and E0 (−38 W m^{-2}). Figure 16 shows the daily mean SWCF and LWCF at the TOA for M0. The sum of SWCF and LWCF is in the range of −20 and −60 W m^{-2} for most days during the 39-day period, which results in the 39-day mean of −39 W m^{-2}. Note that no near cancellation occurs between the SWCF and LWCF at the TOA for either the models M0 and E0 or the FC data; these results contrast with observations from the Earth Radiation Budget Experiment (e.g., Kiehl and Ramanathan 1990; Kiehl 1994). As shown later in section 5c, the enhanced shortwave cloud absorption, which is not considered in the radiation scheme for M0 and E0, may explain this difference. In other words, the enhanced shortwave cloud absorption that is not considered in the radiation scheme may result in the near cancellation.

The smaller ice water path produced in M0 also reduces the magnitude (−110 W m^{-2}) of the SWCF at the surface compared to −121 W m^{-2} in E0. The 39-day mean SWCF at the surface from M0 is comparable to the FC data (−98 W m^{-2}) and other estimates. Chou and Zhao (1997) showed that the SWCF at the surface averaged over the four months during TOGA COARE

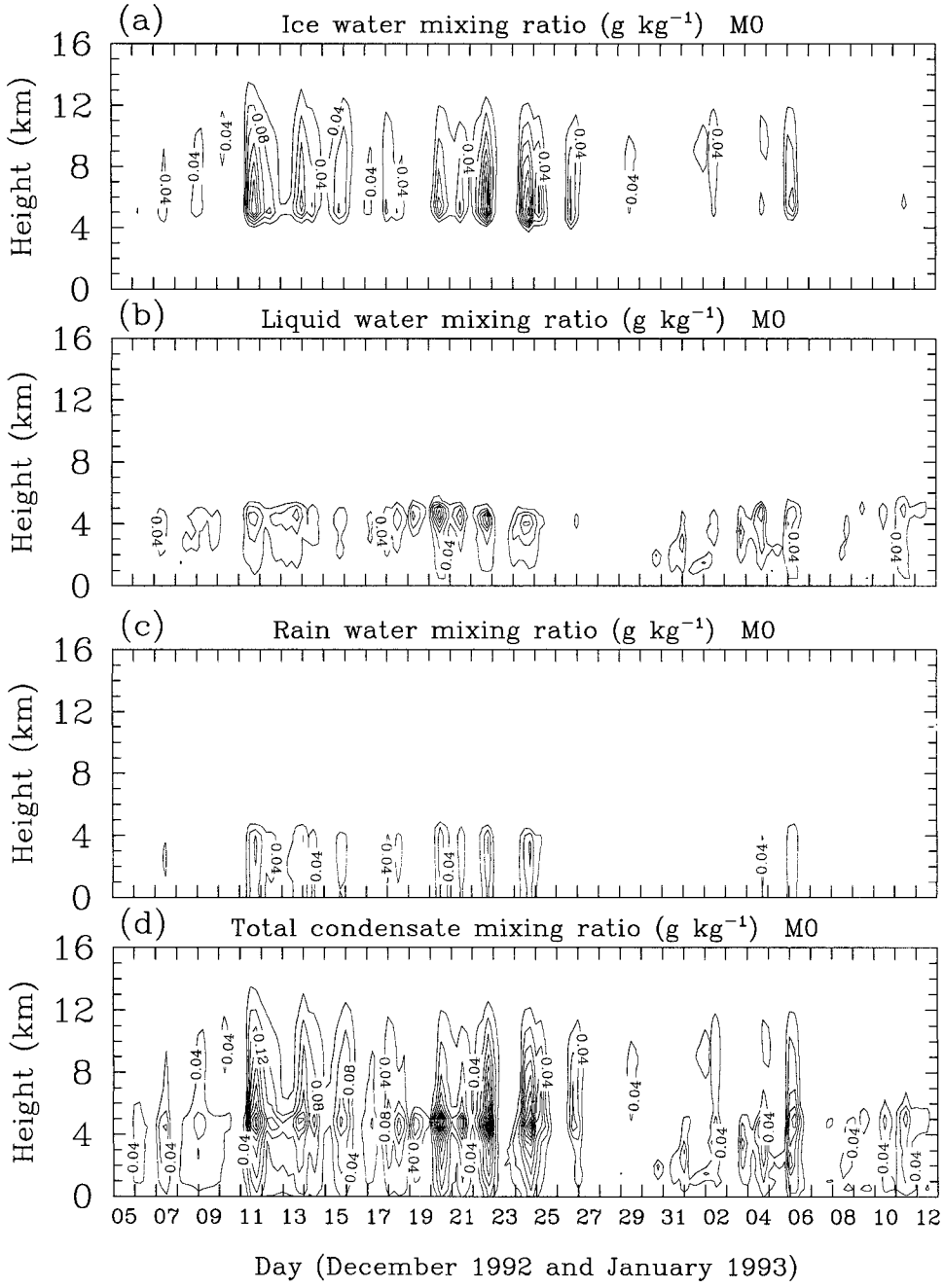

FIG. 10. Evolution of 6-hourly domain-averaged (a) ice water (type A + type B), (b) liquid water, (c) rainwater, and (d) total condensate mixing ratio (g kg^{-1}) from model M0. The melting level is near 5 km. The peak in total condensate mixing ratio is consistent with the bright band observed by the 915-MHz profiler.

and the seven radiation stations is -99 W m^{-2}. The estimates using the IMET buoy surface insolation measurements are -103 and -107 W m^{-2}, using two different methods (Waliser et al. 1996). The LWCF at the surface in M0 is similar to that in E0 and the FC data.

The SWCF and LWCF throughout the atmosphere in Table 1 are obtained by the differences between the SWCF and LWCF at the TOA and at the surface, respectively. The LWCF throughout the atmosphere from M0 is close to that from the FC data. However, the SWCF throughout the atmosphere from both models and the FC data has opposite sign although the magnitudes of the forcing are small, which may be due to the biases in either observations or models.

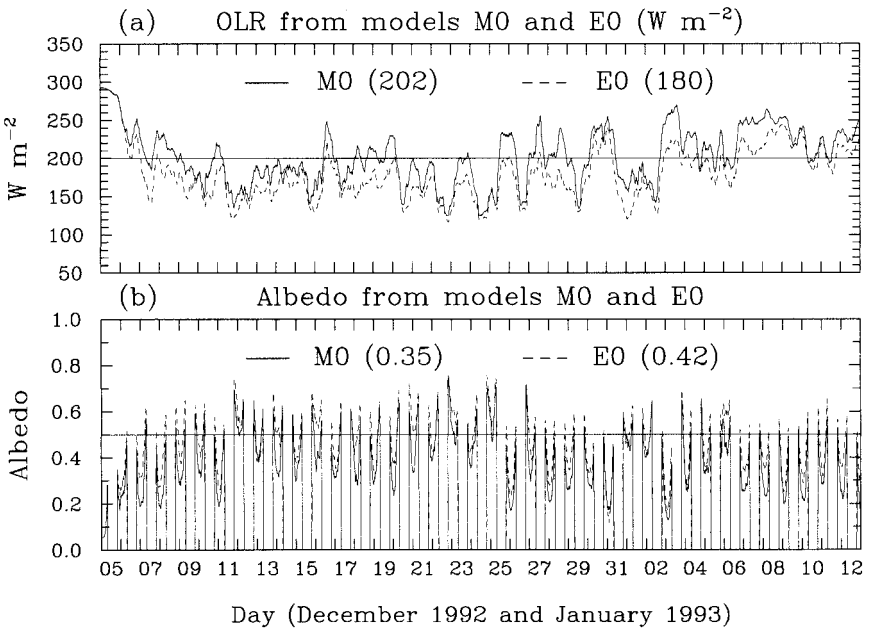

FIG. 11. Evolution of domain-averaged (a) OLR (W m^{-2}) and (b) albedo from models M0 (solid) and E0 (dashed). The temporal interval is 15 min.

f. Surface energy budget

The effects of the modified ice scheme on the surface energy budget is mainly through its influence on the shortwave radiative flux at the surface. Since the surface heat fluxes are calculated using the observed evolving SST data, there is no direct feedback between cloud-scale processes and oceanic processes. But the evolving SST includes the effects of the real cloud systems. Table 2 shows each term in the surface energy budget for M0, E0, and the IMET data. The IMET dataset is the version 2.0b (version 1.0b was used in Part I of this paper) (Weller and Anderson 1996). The reduced ice water path in M0 increases the net shortwave radiative flux (SWF) at the surface from 149.1 W m^{-2} in E0 to 182.9 W m^{-2} in M0. The magnitude of net longwave radiative flux (LWF) at the surface slightly increases from E0 (-39.0 W m^{-2}) to M0 (-46.2 W m^{-2}), which is closer to the IMET data (-54.6 W m^{-2}). The net heat fluxes are similar: -117.7 W m^{-2} (M0), -115.7 W m^{-2} (E0), and -113.3 W m^{-2} (IMET). The net surface budget is 19.0 W m^{-2} from M0, which has the same sign as the net budget from the IMET (10.3 W m^{-2}). The difference of net surface budget (8.7 W m^{-2}) between M0 and IMET is smaller than the uncertainty of IMET data (10 W m^{-2}; Weller and Anderson 1996). The dynamically consistent surface forcing available from the CRM provides an excellent dataset for ocean models to study the warm pool response and the relationship between tropical cloud systems and the SST (e.g., Webster et al. 1996; Anderson et al. 1996). The warm pool response to the surface forcing in a one-dimensional ocean model will be presented in the Part III of this paper.

TABLE 2. Surface energy budgets from M0, E0, and IMET.

Fluxes (W m^{-2})	M0	E0	IMET
LFW_{SRF}	-46.2	-39.0	-54.5
SWF_{SRF}	182.9	149.1	178.2
Q_{lat}	-109.9	-102.4	-102.7
Q_{sen}	-7.8	-13.3	-10.6
Q_{net}	19.0	-5.6	10.3

5. Offline calculations using the radiative transfer model

By offline calculation we mean that the radiative effects are not allowed to feed through the model dynamics, but rather the model fields are used to drive the radiation model. In this section, three offline calculations of radiative properties using the radiative transfer model are discussed to examine the sensitivity of radiative properties to atmospheric properties, and the parameters and processes in the radiation model.

a. Offline calculation R1

The first offline calculation R1 is to examine the consequence of the temperature and moisture biases (as shown in section 3a) on the radiative fluxes. The observed evolving temperature and moisture profiles replace model-produced temperature and moisture fields as the input data, together with the model-produced cloud condensate fields from M0, to force the radiation model. Table 3 lists the net shortwave and longwave radiative fluxes at the TOA, throughout the atmosphere,

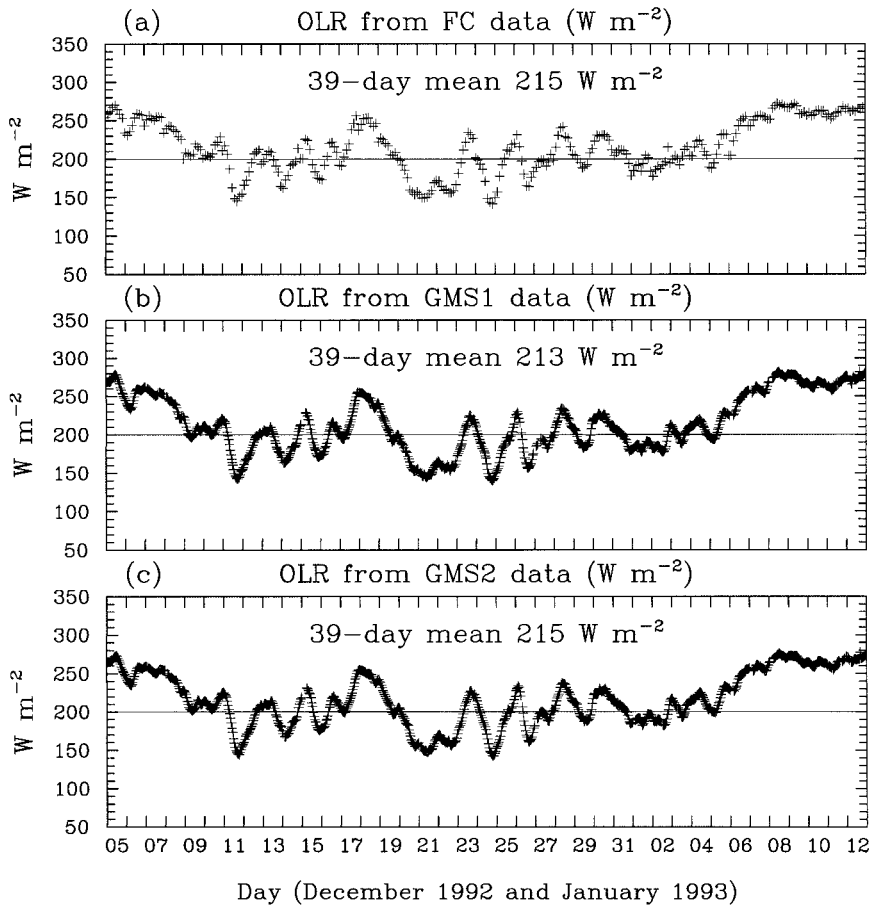

FIG. 12. Evolution of OLR (W m^{-2}) from (a) FC, (b) *GMS-1,* and (c) *GMS-2* averaged over the IFA of TOGA COARE. The 3-hourly FC data have a 2.5° horizontal resolution. The *GMS-1* data have a horizontal resolution of 0.25° and a temporal resolution of about 1 h. The *GMS-2* data have a horizontal resolution of 2.5° and a temporal resolution of 1 h.

and at the surface, respectively (see the definitions in Table 1 of Part I). The temperature and moisture biases have a small effect on the net shortwave radiative fluxes. The warm and moist biases reduce the outgoing longwave radiative fluxes at the TOA by 5 W m^{-2} (from 207 W m^{-2} of R1 to 202 W m^{-2} of M0). The difference between M0 and R1 is larger during the undisturbed period than during the disturbed period because the temperature and moisture biases are larger during the undisturbed period. The 9 W m^{-2} decrease in the atmospheric net shortwave and longwave forcing (SWF_{ATM} + LWF_{ATM}) due to using the observed temperature and water vapor mixing ratio fields in R1 would produce a tropospheric cooling of more than 3 K over the 39-day period relative to that of M0. Since the condensate fields (type-A ice and liquid water) used in M0 and R1 are the same, there is virtually no difference for the cloud radiative forcing between M0 and R1 (Table 4).

b. Offline calculation R2

The second offline calculation R2 is designed to test the effects of ice particle size on the radiative fluxes. The effective radius of ice particles used in R2 is 60 μm (compared to 30 μm used in M0). Table 3 shows that the net shortwave and longwave radiative fluxes are modified by doubling the effective radius of ice particles in the radiation scheme. The doubled effective radius in R2 reduces the reflected solar flux at the TOA and therefore increases the net shortwave radiative flux and decreases the albedo, because the incoming solar flux is the same for R2 and M0. The 39-day mean albedo (0.31) in R2 is the same as the albedo from the GMS2 data. However, the decreased reflected solar flux at the TOA results in the increase of downward solar flux and net shortwave radiative flux at the surface (196 W m^{-2}), which exceeds the IMET measurement (178 W m^{-2}) by 18 W m^{-2}. The net shortwave radiative flux throughout the atmosphere is about the same for R2 and M0. The impact of doubled effective radius on the longwave fluxes occurs mostly at the TOA and throughout the atmosphere. The 39-day mean OLR increases to 215 W m^{-2}, which is close to all three observational datasets.

The influence of doubled effective radius on the cloud radiative forcing is shown in Table 4. The modification

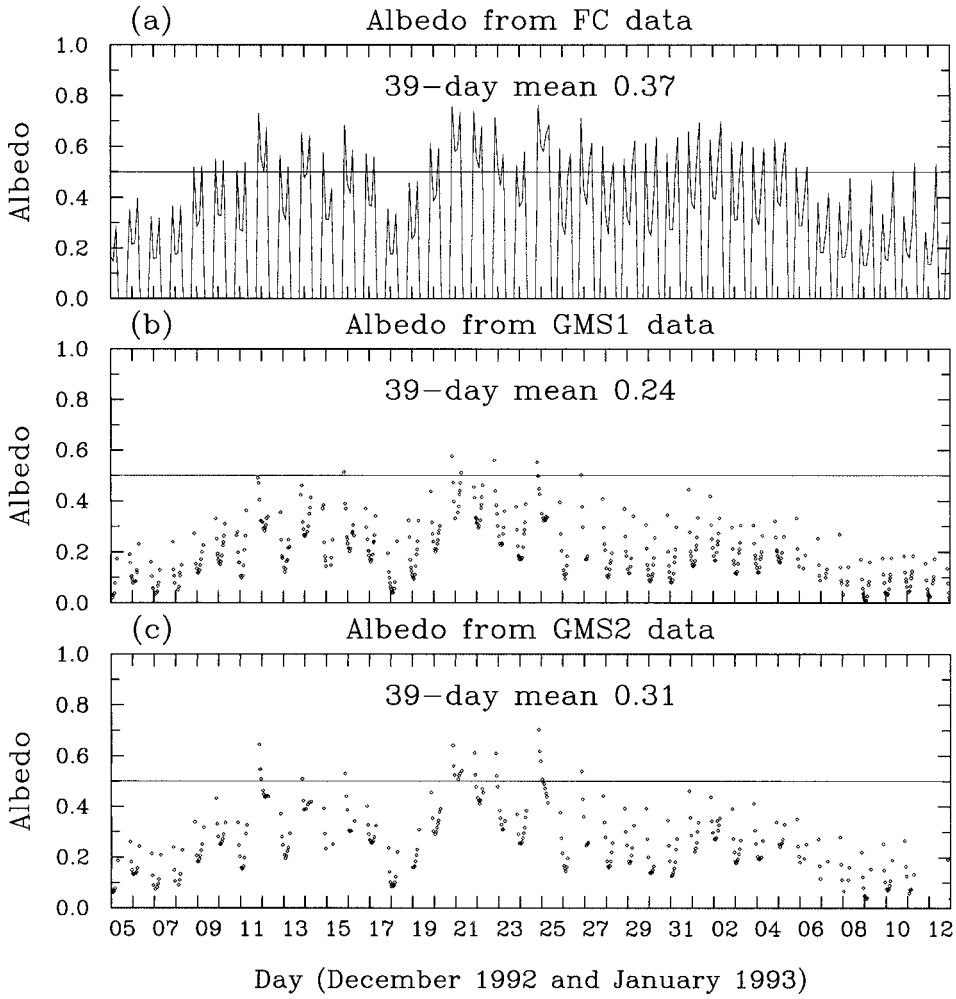

FIG. 13. Evolution of albedo from (a) FC, (b) *GMS-1,* and (c) *GMS-2.*

of shortwave and longwave cloud forcing is almost offset, and the net cloud radiative forcing (SWCF + LWCF) at the TOA in R2 (-36 W m^{-2}) is similar to that in M0 (-39 W m^{-2}). But the net cloud radiative forcing at the surface is different mainly due to the modified shortwave cloud forcing. The doubled effective radius reduces the shortwave cooling effects from clouds, and the 39-day mean SWCF at the surface is -101 W m^{-2} in R2, which is close to other estimates obtained for TOGA COARE. These results suggest that the radiative fluxes and cloud radiative forcing are sensitive to the effective radius of ice particles prescribed in the radiation scheme. This is consistent with the result obtained by Fu et al. (1995) who showed the sensitivity of radiative fluxes and cloud forcing due to changes in effective radius of ice particles in a series of short-term (12 h) fully interactive simulations of a tropical squall line. The results also suggest a special need for obtaining the measurement of ice particle size in different cloud systems from field experiments.

Since the offline calculation does not permit the effects of radiative fluxes to feed back onto cloud system properties, several short 7-day simulations during the strong forcing period (19–25 December 1992) were performed with the cloud-interactive radiation parameterization using either 60 or 30 μm for the effective radii of ice particles. It is found that, when using the same ice particle size (60 μm), the radiative fluxes from the interactive simulation are similar to those from the offline calculation, which uses the temperature, moisture, and condensate fields from the 30-μm interactive one.

c. Offline calculation R3

The third offline calculation R3 investigates the effects of enhanced shortwave cloud absorption on the radiation calculation (e.g., Cess et al. 1995; Kiehl et al. 1995). While this issue is very controversial, the CRM approach can be used to estimate its effect because the CRM allows the explicit cloud–radiation interaction through cloud-scale dynamics, which is not explicitly present in GCMs. The effective radius of 60 μm is used

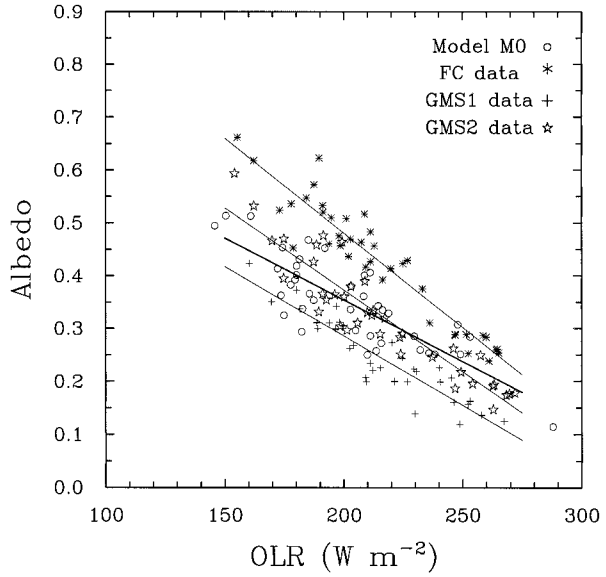

FIG. 14. Daily-mean albedo vs OLR for M0, FC, *GMS-1,* and *GMS-2.* Thick solid line is the least squares regression fit for M0, and thin solid lines are the least squares regression fits for FC, *GMS-1,* and *GMS-2,* respectively.

in R3 for ice particles. The procedure for enhancing shortwave cloud absorption follows that in Kiehl et al. (1995), namely, by changing the values of single-scattering albedo in the radiation scheme. The shortwave fluxes and cloud forcing are significantly changed by the enhanced shortwave cloud absorption, as shown in Tables 3 and 4. The net shortwave flux at the surface is 186 W m^{-2} (compared to 178 W m^{-2} from IMET), which is smaller than 196 W m^{-2} of R2 because of the large increase of the net shortwave flux throughout the atmosphere due to the enhanced shortwave cloud absorption (132 W m^{-2} in R3 compared to 98 W m^{-2} in R2). The 39-day mean albedo from R3 decreases to 0.26, which is close to 0.24 from the *GMS-1* data. In this case both the doubled effective radius and the enhanced shortwave cloud absorption result in the net shortwave flux closer to observations at both the TOA and surface.

As expected, by including the enhanced shortwave cloud absorption in the radiation scheme, the shortwave cloud forcing in R3 is modified. The shortwave cloud forcing at the TOA becomes much smaller (-73 W m^{-2}), and the shortwave cloud forcing at the surface is -112 W m^{-2} (Table 4). These give a ratio of 1.53, which is an indicator for the enhanced shortwave cloud absorption (Cess et al. 1995). With the decrease of shortwave cloud forcing, the net shortwave and longwave cloud forcing at the TOA is closer to the near cancellation in R3 (-16 W m^{-2}) than in R2 (-36 W m^{-2}) and M0 (-39 W m^{-2}). Evidently, the shortwave warming effect from clouds increases throughout the atmosphere and is about the same as the longwave warming effect from clouds in R3.

We also performed several short 7-day simulations during the strong forcing period (19–25 December 1992) using the cloud-interactive radiation parameterization schemes with or without the enhanced shortwave cloud absorption. We found that the radiative fluxes from the interactive run with the enhanced absorption are about the same as those from the offline calculation with the enhanced absorption, which uses the temperature, moisture, and condensate fields from the run without the enhanced absorption. This is because the change of radiative heating rate by the doubled effective radius of ice particles and the enhanced shortwave cloud absorption is small compared to the large-scale forcing imposed in the simulation. The doubled effective radius and the enhanced shortwave cloud absorption in the radiation scheme have small impacts on the temperature, moisture, and cloud condensate fields based on the 7-day simulations.

6. Discussion and summary

One of the uncertainties in cloud-resolving models concerns the microphysical parameterization. Since cloud condensate data are not presently available from observations, the modeled cloud condensate fields cannot be directly evaluated. However, the long-term simulation of cloud systems provides an opportunity to indirectly verify the modeled fields through employing the satellite-observed radiative flux. The quantitative comparison between the 39-day simulation (E0) and observations in the Part I of this paper suggested that Koenig and Murray's original ice parameterization produced excessive cirrus and caused the discrepancy between the modeled and observed radiative properties. This motivated us to use (albeit limited) microphysical measurements from CEPEX as a justification for changing the terminal velocity of ice particles. The modeled ice sedimentation flux is found to be much too small when compared to observations. To eliminate this deficiency, the representation of ice fall speed used in Koenig and Murray's ice scheme was modified. The three-class or four-class ice schemes are arguably more physically complete than two-class ice schemes. However, Koenig and Murray's two-class ice scheme predicted both the mixing ratio and the number concentration while most of three-class ice schemes predicted only the mixing ratio. The lack of observational data and uncertainties associated with physical processes also make it more difficult to verify the modeled ice fields with three-class ice schemes. As shown in the GCSS intercomparison project (Moncrieff et al. 1997; Krueger 1996), different cloud properties and radiative properties were produced by various three-class ice schemes.

Instead of comparing different ice schemes, we focus on the effects of ice microphysics on the simulation of cloud properties and radiative properties using the Koenig and Murray's two-class ice scheme. In a separate paper, a sensitivity study is conducted to examine the effects of extreme change of cloud microphysical pro-

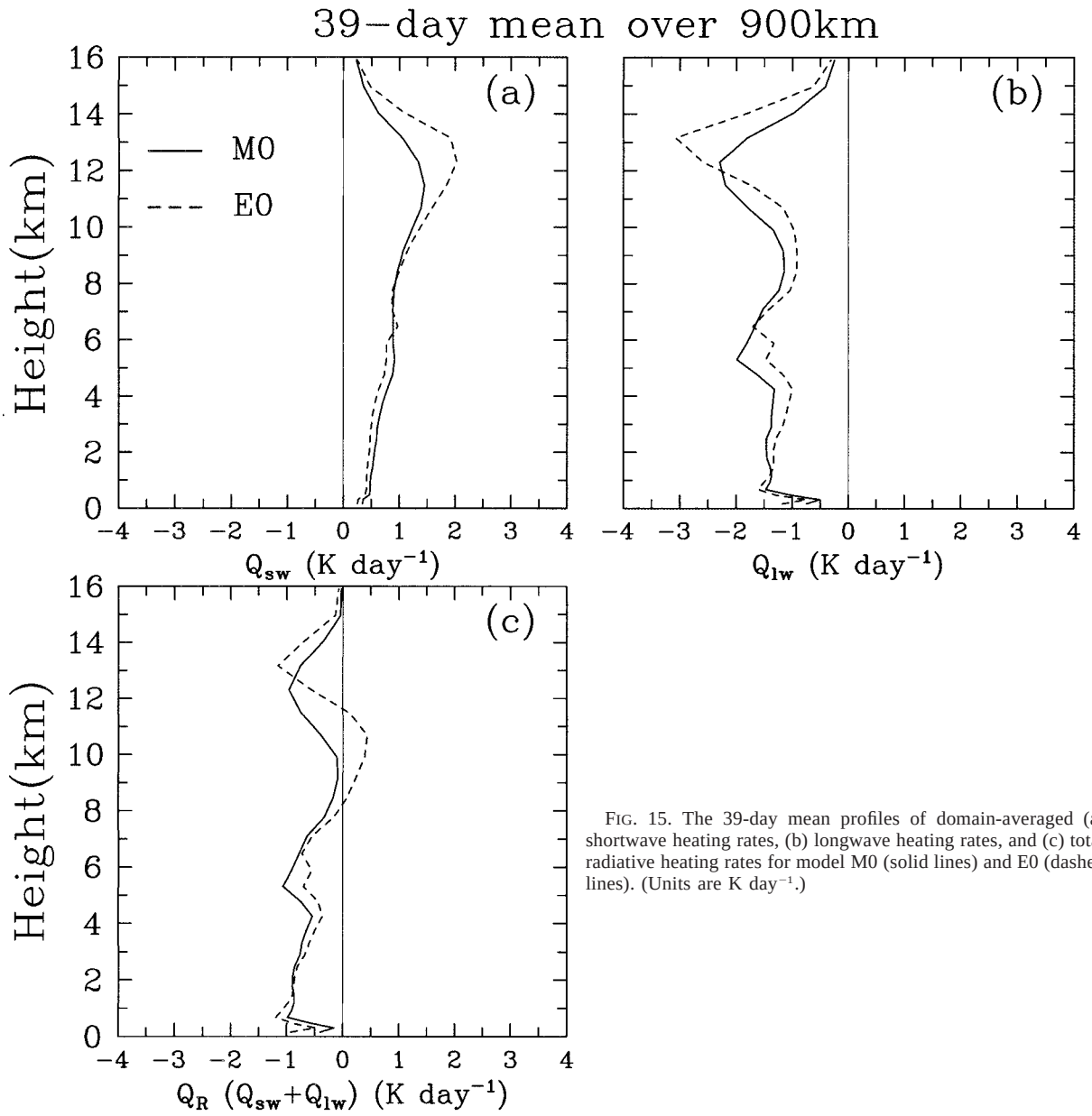

FIG. 15. The 39-day mean profiles of domain-averaged (a) shortwave heating rates, (b) longwave heating rates, and (c) total radiative heating rates for model M0 (solid lines) and E0 (dashed lines). (Units are K day^{-1}.)

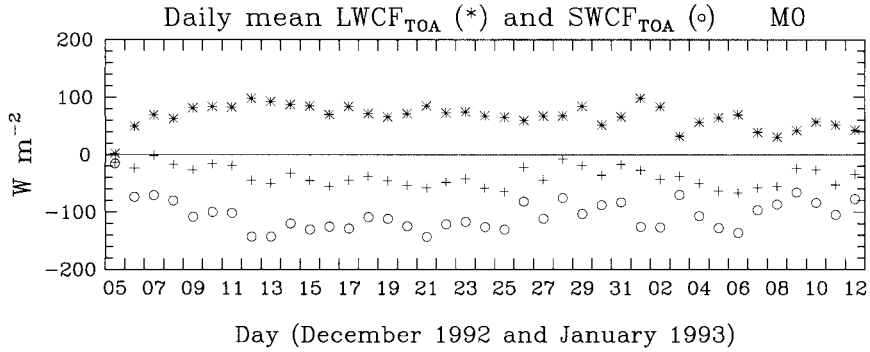

FIG. 16. Evolution of daily domain-averaged longwave cloud forcing (*), shortwave cloud forcing (○), and the sum (+) for M0. (Units are W m^{-2}.).

TABLE 3. Radiative forcing (W m^{-2}) from M0, R1, R2, and R3.

Radiative forcing	M0	R1	R2	R3
SWF_{TOA} (albedo)	278 (0.35)	277 (0.35)	294 (0.31)	318 (0.26)
LWF_{TOA} (−OLR)	−202	−207	−215	−215
SWF_{ATM}	95	93	98	132
LWF_{ATM}	−156	−163	−168	−168
SWF_{SRF}	183	184	196	186
LWF_{SRF}	−46	−44	−47	−47

TABLE 4. Cloud radiative forcing (W m^{-2}) from M0, R1, R2, and R3.

Cloud radiative forcing	M0	R1	R2	R3
$SWCF_{TOA}$	−105	−105	−93	−73
$LWCF_{TOA}$	66	69	57	57
$SWCF_{ATM}$	5	6	8	39
$LWCF_{ATM}$	48	48	38	38
$SWCF_{SRF}$	−110	−111	−101	−112
$LWCF_{SRF}$	18	21	19	19

cesses on the simulation of the Global Atmospheric Research Programme Atlantic Tropical Experiment cloud systems (Grabowski et al. 1999). It should be pointed out that the generalization of the modification of the ice fall speed for cloud systems over different regions and other two-class and three-class schemes required further studies because of the different features of ice particles and the different treatment of ice particles in the ice schemes.

A new 39-day simulation (M0) is performed using the modified ice parameterization and the nonlocal boundary layer diffusion scheme and is compared with the 39-day simulation (E0) presented in Part I. The results show that the overall performance of the cloud-resolving model is improved with the modified ice scheme. The impact of cloud physics on thermodynamical, condensate, and radiation fields is clearly illustrated by the comparison between M0 and E0. More realistic microphysical properties, cloud properties, and radiative properties are simulated and are comparable with the limited observations. Much smaller ice water path is produced in M0, which results in the increase of OLR and the decrease of albedo and surface shortwave cloud forcing. The 39-day mean value of OLR (202 W m^{-2}) is closer to the values from three different observational datasets. The 39-day mean surface shortwave cloud forcing (−110 W m^{-2}) is comparable with other estimates obtained for TOGA COARE. The 39-day mean values of surface net longwave, shortwave, latent, and sensible fluxes are −46.2, 182.9, −109.9, and −7.8 W m^{-2}, respectively, also in line with the IMET data (−54.6, 178.2, −102.7, and −10.6 W m^{-2}).

An interesting feature arises from the albedo comparison between the model and observations. The 39-day mean value of albedo from M0 is 0.35, which is smaller than 0.37 from the FC, larger than 0.31 from GMS2, and larger than 0.24 from GMS1. As shown in the offline calculations, small values of the albedo are indicative of the larger effective radius of ice particles and enhanced shortwave cloud absorption. Careful observational analyses are required before these sensitivities can be fully understood.

From the offline radiation calculations as well as the cloud-interactive radiation simulations, we found that the radiative flux and cloud radiative forcing are sensitive to the doubled effective radius of ice particles and the enhanced shortwave cloud absorption, while the cloud properties are less affected by the changes of these parameters in the radiation scheme. In the context of large-domain and finescale simulation that imposes a large-scale forcing but resolves the cloud dynamics, the magnitude of radiative heating rate change due to the modification of parameters in the radiation scheme is relatively small and does not much affect the simulated cloud systems. Nevertheless, it should be borne in mind that our objectives center on parameterization issues, in which case the collective effects of clouds and cloud–radiation interaction are paramount.

The long-term cloud properties generated from this simulation are currently being used by several radiation groups to improve the parameterization of cloud radiative properties in general circulation models. The special design of the cloud-resolving modeling allows the mutual and direct interactions among observation, cloud-scale, and large-scale groups. The further improvement of the simulation of cloud systems clearly requires high-quality microphysical (ice particle size and ice fall speed), cloud condensate (ice water and liquid water mixing ratio retrieved from the 915-MHz profiler), and radiation data (broadband albedo and cloud radiative forcing at the TOA), and points to the need for new and more comprehensive observations.

Acknowledgments. We would like to thank Greg McFarquhar and Andy Heymsfield for providing the CEPEX data and for discussion on the ice parameterization. Personal review of the manuscript by Andy Heymsfield and Jim Hack are gratefully acknowledged. Comments by Steve Krueger and two reviewers greatly improved the presentation of results. This work was supported by NSF Grant ATM-9525857 and is part of the NCAR Clouds in Climate Program.

REFERENCES

Anderson, S. P., R. A. Weller, and R. Lukas, 1996: Surface buoyancy forcing and the mixed layer of the western Pacific warm pool: Observations and 1D model results. *J. Climate,* **9,** 3056–3085.

Cess, R. D., and Coauthors, 1995: Absorption of solar radiation by clouds: Observations versus models. *Science,* **267,** 496–499.

Chin, H.-N., 1994: The impact of the ice phase and radiation on a midlatitude squall line system. *J. Atmos. Sci.,* **51,** 3320–3343.

Chou, M.-D., and W. Zhao, 1997: Estimation and model validation

of surface solar radiation and cloud radiative forcing using TOGA COARE measurements. *J. Climate,* **10,** 610–620.

Clark T. L., W. D. Hall, and J. L. Coen, 1996: Source code documentation for the Clark-Hall cloud-scale model: Code version G3CH01. NCAR Tech. Note NCAR/TN-426+STR, 137 pp. [Available from NCAR Information Service, P. O. Box 3000, Boulder, CO 80307.]

Collins, W. D., A. Bucholtz, and F. P. J. Valero, 1997: Derivation of top-of-atmosphere fluxes from geostationary satellites using high-altitude aircraft measurements: Results from COARE and CEPEX. Preprints, *Ninth Conf. on Atmospheric Radiation,* Long Beach, CA, Amer. Meteor. Soc., 198–202.

Cotton, W. R., M. A. Stephens, T. Nehrkorn, and G. J. Tripoli, 1982: The Colorado State University three-dimensional cloud-mesoscale model-1982. Part II: An ice-phase parameterization. *J. Rech. Atmos.,* **16,** 295–320.

Dudhia, J., 1989: Numerical study of convection observed during the Winter Monsoon Experiment using a mesoscale two-dimensional model. *J. Atmos. Sci.,* **46,** 3077–3107.

Fairall, C. W., E. F. Bradley, D. P. Rogers, J. B. Edson, and G. S. Young, 1996: Bulk parameterization of air-sea fluxes for Tropical Ocean-Global Atmosphere Coupled Ocean–Atmosphere Response Experiment. *J. Geophys. Res.,* **101,** 3747–3764.

Ferrier, B. S., 1994: A double-moment multiple-phase four-class bulk ice scheme. Part I: Description. *J. Atmos. Sci.,* **51,** 249–280.

——, W.-K. Tao, and J. Simpson, 1995: A double-moment multiple-phase four-class bulk ice scheme. Part II: Simulations of convective storms in different large-scale environments and comparisons with other bulk parameterizations. *J. Atmos. Sci.,* **52,** 1001–1033.

Fovell, R. G., and Y. Ogura, 1988: Numerical simulation of a midlatitude squall line in two dimensions. *J. Atmos. Sci.,* **45,** 3846–3879.

Fowler, L. D., D. A. Randall, and S. A. Rutledge, 1996: Liquid and ice cloud microphysics in the CSU general circulation model. Part I: Model description and simulated microphysical processes. *J. Climate,* **9,** 489–529.

Fu, Q., S. K. Krueger, and K. N. Liou, 1995: Interaction of radiation and convection in simulated tropical cloud clusters. *J. Atmos. Sci.,* **52,** 1310–1328.

Gage, K. S., C. R. Williams, and W. L. Ecklund, 1994: UHF wind profilers: A new tool for diagnosing tropical convective cloud systems. *Bull. Amer. Meteor. Soc.,* **75,** 2289–2294.

GCSS Science Team, 1993: The GEWEX Cloud System Study. *Bull. Amer. Meteor. Soc.,* **74,** 387–400.

Grabowski, W. W., X. Wu, and M. W. Moncrieff, 1996: Cloud resolving modeling of tropical cloud systems during Phase III of GATE. Part I: Two-dimensional experiments. *J. Atmos. Sci.,* **53,** 3684–3709.

——, ——, and ——, 1999: Cloud resolving modeling of tropical cloud systems during Phase III of GATE. Part III: Effects of cloud microphysics. *J. Atmos. Sci.,* **56,** 2384–2402.

Heymsfield, A. J., and L. J. Donner, 1990: A scheme for parameterizing ice-cloud water content in general circulation models. *J. Atmos. Sci.,* **47,** 1865–1877.

Holtslag, A. A. M., and C.-H. Moeng, 1991: Eddy diffusivity and countergradient transport in the convective atmospheric boundary layer. *J. Atmos. Sci.,* **48,** 1690–1698.

Hong, S.-Y., and H.-L. Pan, 1996: Nonlocal boundary layer vertical diffusion in a medium-range forecast model. *Mon. Wea. Rev.,* **124,** 2322–2339.

Kessler, E., 1969: On the distribution and continuity of water substance in atmospheric circulations. *Meteor. Monogr.,* No. 32, Amer. Meteor. Soc., 84 pp.

Kiehl, J. T., 1994: On the observed near cancellation between longwave and shortwave cloud forcing in tropical regions. *J. Climate,* **7,** 559–565.

——, and V. Ramanathan, 1990: Comparison of cloud forcing derived from the Earth Radiation Budget Experiment with that simulated by the NCAR Community Climate Model. *J. Geophys. Res.,* **95,** 11 679–11 698.

——, J. J. Hack, and B. P. Briegleb, 1994: The simulated Earth radiation budget of the National Center for Atmospheric Research community climate model CCM2 and comparisons with the Earth Radiation Budget Experiment (ERBE). *J. Geophys. Res.,* **99,** 20 815–20 827.

——, ——, M. H. Zhang, and R. D. Cess, 1995: Sensitivity of a GCM climate to enhanced shortwave cloud absorption. *J. Climate,* **8,** 2200–2212.

——, J. J. Hack, G. B. Bonan, B. B. Boville, D. L. Williamson, and P. J. Rasch, 1998: The National Center for Atmospheric Research Community Climate Model: CCM3. *J. Climate,* **11,** 1131–1149.

Koenig, L. R., and F. W. Murray, 1976: Ice-bearing cumulus clouds evolution: Numerical simulation and general comparison against observations. *J. Appl. Meteor.,* **15,** 747–762.

Krueger, S. K., 1996: A GCSS intercomparison of cloud-resolving models based on TOGA COARE observations. *Proc. Workshop on New Insights and Approaches to Convective Parameterization,* Reading, United Kingdom, ECMWF, 113–127.

——, Q. Fu, K. N. Liou, and H.-N. Chin, 1995: Improvments of an ice-phase microphysics parameterization for use in numerical simulations of tropical convection. *J. Appl. Meteor.,* **34,** 281–287.

Lin X., and R. H. Johnson, 1996: Kinematic and thermodynamic characteristics of the flow over the western Pacific warm pool during TOGA COARE. *J. Atmos. Sci.,* **53,** 695–715.

Lin, Y.-L., R. D. Farley, and H. D. Orville, 1983: Bulk parameterization of the snow field in a cloud model. *J. Climate Appl. Meteor.,* **22,** 1065–1092.

Liu, C.-H., M. W. Moncrieff, and E. J. Zipser, 1997: Dynamical influence of microphysics in tropical squall line: A numerical study. *Mon. Wea. Rev.,* **125,** 2193–2210.

McCumber, M., W.-K. Tao, J. Simpson, R. Penc, and S.-T. Soong, 1991: Comparison of ice-phase microphysical parameterization schemes using numerical simulations of convection. *J. Appl. Meteor.,* **30,** 985–1004.

McFarquhar, G. M., and A. J. Heymsfield, 1996: Microphysical characteristics of three cirrus anvils sampled during the Central Equatorial Pacific Experiment. *J. Atmos. Sci.,* **53,** 2401–2423.

Minnis, P., and E. F. Harrison, 1984: Diurnal variability of regional cloud and clear-sky radiative parameters derived from GOES data. Part III: November 1978 radiative parameters. *J. Climate Appl. Meteor.,* **23,** 1032–1051.

Moncrieff, M. W., S. K. Krueger, D. Gregory, J.-L. Redelsperger, and W.-K. Tao, 1997: GEWEX Cloud System Study (GCSS) Working Group 4: Precipitating convective cloud systems. *Bull. Amer. Meteor. Soc.,* **78,** 831–845.

Nicholls, M. E., 1987: A comparison of the results of a two-dimensional numerical simulation of a tropical squall line with observations. *Mon. Wea. Rev.,* **115,** 3055–3077.

Ramanathan, V., E. J. Pitcher, R. C. Malone, and M. L. Blackmon, 1983: The response of a spectral general circulation model to refinements in radiative processes. *J. Atmos. Sci.,* **40,** 605–630.

Rutledge, S. A., and P. V. Hobbs, 1983: The mesoscale and microscale structure and organization of clouds and precipitation in midlatitude cyclones. Part VIII: A model for the ''seeder-feeder'' process in warm-frontal rainbands. *J. Atmos. Sci.,* **40,** 1185–1206.

Slingo, J. M., 1987: The development and verification of a cloud prediction scheme for the ECMWF model. *Quart. J. Roy. Meteor. Soc.,* **113,** 899–927.

Smagorinsky, J., 1963: General circulation experiments with the primitive equations. I. The basic experiment. *Mon. Wea. Rev.,* **91,** 99–164.

Tao, W.-K., and J. Simpson, 1989: Modeling study of a tropical squall-type convective line. *J. Atmos. Sci.,* **46,** 177–202.

——, J. Scala, B. S. Ferrier, and J. Simpson, 1995: The effects of melting processes on the development of a tropical and a midlatitude squall line. *J. Atmos. Sci.,* **52,** 1934–1948.

Troen, I., and L. Mahrt, 1986: A simple model of the atmospheric boundary layer: Sensitivity to surface evaporation. *Bound.-Layer Meteor.,* **37,** 129–148.

Waliser, D. E., W. D. Collins, and S. P. Anderson, 1996: An estimate of the surface shortwave cloud forcing over the western Pacific during TOGA COARE. *Geophys. Res. Lett.,* **23,** 519–522.

Webster, P. J., C. A. Clayson, and J. A. Curry, 1996: Clouds, radiation, and the diurnal cycle of sea surface temperature in the tropical western Pacific. *J. Climate,* **9,** 1712–1730.

Weller, R. A., and S. P. Anderson, 1996: Surface meteorology and air–sea fluxes in the western equatorial Pacific warm pool during the TOGA Coupled Ocean–Atmosphere Response Experiment. *J. Climate,* **9,** 1959–1990.

Williams, S. F., 1993: Central Equatorial Pacific Experiment (CEPEX) operations summary. UCAR Office of Field Project Support, 321 pp. [Available from UCAR Office of Field Project Support, P.O. Box 3000, Boulder, CO 80307.]

Wu, X., and M. W. Moncrieff, 1996: Collective effects of organized convection and their approximation in general circulation models. *J. Atmos. Sci.,* **53,** 1477–1495.

——, W. W. Grabowski, and M. W. Moncrieff, 1998: Long-term behavior of cloud systems in TOGA COARE and their interactions with radiative and surface processes. Part I: Two-dimensional modeling study. *J. Atmos. Sci.,* **55,** 2693–2714.

Yoshizaki, M., 1986: Numerical simulations of tropical squall-line clusters: Two-dimensional model. *J. Meteor. Soc. Japan,* **64,** 469–491.

Zhang, Y.-C., W. B. Rossow, and A. A. Lacis, 1995: Calculation of surface and top of atmosphere radiative fluxes from physical quantities based on ISCCP datasets, 1. Method and sensitivity to input data uncertainties. *J. Geophys. Res.,* **100,** 1149–1165.